RESEARCH ARTICLE

ULTRAFAST OPTICS

All-optical control and metrology of electron pulses

C. Kealhofer,[1,2] W. Schneider,[1,2] D. Ehberger,[1,2] A. Ryabov,[1,2] F. Krausz,[1,2]* P. Baum[1,2]*

Short electron pulses are central to time-resolved atomic-scale diffraction and electron microscopy, streak cameras, and free-electron lasers. We demonstrate phase-space control and characterization of 5-picometer electron pulses using few-cycle terahertz radiation, extending concepts of microwave electron pulse compression and streaking to terahertz frequencies. Optical-field control of electron pulses provides synchronism to laser pulses and offers a temporal resolution that is ultimately limited by the rise-time of the optical fields applied. We used few-cycle waveforms carried at 0.3 terahertz to compress electron pulses by a factor of 12 with a timing stability of <4 femtoseconds (root mean square) and measure them by means of field-induced beam deflection (streaking). Scaling the concept toward multiterahertz control fields holds promise for approaching the electronic time scale in time-resolved electron diffraction and microscopy.

Electron beams controlled with temporally varying electric fields enabled the first oscilloscopes and electronic computers; today, they are essential to free-electron lasers (*1*, *2*), ultrafast streak cameras (*3*–*5*), and femtosecond imaging and diffraction techniques (*6*–*8*). Microwave technology at gigahertz frequencies has been the workhorse for ultrafast electron pulse control thus far, with applications ranging from particle acceleration to ultrafast pulse compression and high-resolution streak cameras. Unfortunately, microwave components suffer from appreciable phase drifts, and laser-microwave synchronization below 10 fs becomes technologically challenging (*9*–*11*). Laser field–driven dielectric accelerator structures operating near petahertz frequencies are being developed for next-generation particle accelerators (*12*, *13*), but the short wavelength (~1 μm) and oscillation period (~1 fs) place extreme requirements on the input beam emittance and pulse duration (*12*, *13*). In between, there is the regime of terahertz frequencies. Femtosecond laser–generated plasma waves exhibit terahertz longitudinal fields, which can accelerate electrons efficiently to the relativistic and ultrarelativistic energy domain (*14*). However, the excessive energy, divergence, and insufficient timing control of the resultant several- to multi–megaelectron volt electron pulses impair their utility for most of the above applications and particularly for ultrafast electron diffraction and microscopy.

Pulsed terahertz fields can be generated in a much more controlled way from the coherent nonlinear polarization of matter, such as by optical rectification (*15*). The pulses can reach field strengths on the order of 10^{10} V/m (*16*), and their half-cycle durations ideally match practical electron bunch dimensions (femtosecond-picosecond in time and micrometer-millimeter in diameter). In addition, terahertz control fields derived from a single ultrafast laser via nonlinear optics result in near-perfect (potentially subfemtosecond) temporal synchronization, offering the potential to substantially surpass the performance of microwave-laser synchronization and obviating the need for locking electronics. Therefore, terahertz and infrared radiation generated from laser-driven coherent nonlinear polarization is ideally suited for controlling electron pulses, as indicated by simulations (*17*–*21*) and recent experiments on controlling nanoscale photoemission (*22*) and electron acceleration in a dielectric waveguide (*23*).

Concept and implementation

The experimental implementation of our terahertz-field–controlled electron beamline is depicted in Fig. 1 and consists of two functional units, one for pulse compression and one for temporal characterization by streaking (*24*). Near-1-ps pulses from a ytterbium:yttrium aluminum garnet (Yb:YAG)–based regenerative amplifier (*25*) drive two optical rectification stages for generating few-cycle terahertz pulses. With the same laser, electron pulses with on average approximately one electron per pulse are generated by two-photon photoemission from a gold thin-film photocathode and electrostatically accelerated to 70 keV. The optical rectification stages produce near-single-cycle pulses at a carrier frequency of 0.3 THz with pulse energies up to 40 nJ, implying field strengths of up to ~10^6 V/m under gentle focusing conditions. These are used to control the electron pulse's momentum, energy, duration, or timing.

We used butterfly-shaped metal resonators (Fig. 1, inset) to mediate the interaction between the electrons and the terahertz fields. The terahertz electric field is enhanced in the plane of the resonators and confined to subwavelength dimensions so that energy and momentum conservation in the electron-photon interaction can be satisfied (*26*).

Electrons passing through the resonator structures experience a net change in momentum that corresponds to the integral of the Lorentz force along their trajectories. This change varies sinusoidally as a function of arrival time of the electron in the terahertz field. The first terahertz control stage uses a tilted resonator to provide force components longitudinal to the electron beam for temporal compression. The second terahertz control stage, oriented normal to the beam, provides a delay-dependent deflection for temporal characterization.

The root-mean-square (RMS) electron beam radius is 3 μm at the compression resonator and 11 μm at the streaking resonator, at least 8 times smaller than the resonator mode dimensions. Because the electron pulse from the source is shorter than 1 ps and hence shorter than the half cycle of the terahertz field, the latter exerts a uniform but time-dependent force on the electron wavepacket in all dimensions. This force imparts acceleration and/or compression at the first stage and time-dependent deflection (streaking) at the second stage. As a result, the pulsed electron beam is entirely under the control of a single intense-pulse laser system and its optical fields.

Electron pulse compression

Even without any space charge, electron pulses unavoidably have a finite duration after acceleration because of dispersion (*27*). Electron pulse compression is therefore indispensable for reaching subphonon or electronic time scales in diffraction (*28*). Electron pulse compression requires deceleration and acceleration of the electron when arriving before or after the mean electron arrival time, respectively. For pulse compression with terahertz fields, the first butterfly microstructure is oriented at an angle of 45° with respect to the electron beam. Terahertz pulses are incident at an angle of 45° at the metal surface and hence normal to the electron beam (Fig. 1), so that the terahertz-excited resonance provides time-dependent force components parallel to the electron beam. In analogy to microwave compression, the time-dependent fields permit compression of the electron pulse substantially below its initial duration (*28*) and hence down to attosecond duration in the absence of space charge (*27*). In the limit of one- or few-electron pulses, the pulse duration is understood as the ensemble distribution of electron arrival times with respect to the laser reference.

The effective strength of the compression stage is quantified by g_E, the energy imparted to the electrons in the forward direction with changing delay time. In the experiment, g_E is proportional to the incoming terahertz peak field strength divided by the cycle period. After the interaction, the electron pulse becomes shorter as it propagates, reaching a minimum duration at a distance

$$f_c = m_e(\gamma\beta c)^3/g_E \quad (1)$$

[1]Ludwig-Maximilians-Universität München, Am Coulombwall 1, 85748 Garching, Germany. [2]Max-Planck-Institute of Quantum Optics, Hans-Kopfermann-Straße 1, 85748 Garching, Germany. *Corresponding author. Email: ferenc.krausz@lmu.de (F.K.); peter.baum@lmu.de (P.B.)

where c is the speed of light, m_e is the mass of the electron, β is the ratio of the electron speed to the speed of light, and $\gamma = 1/\sqrt{(1-\beta^2)}$. Localized terahertz fields enhanced to merely 10^6 V/m are sufficient to yield a g_E of 50 eV/ps and hence produce a convenient temporal focus at a distance of tens of centimeters from the compression stage, depending on central energy (*24*).

Temporal characterization

To measure the temporal profile of the electron pulse, the second stage is configured to provide a terahertz-driven delay-dependent deflection, which we dub "streaking," in analogy to microwave-driven and laser field–driven devices. We first tested the temporal characterization with the uncompressed pulse. The time-dependent deflection of the beam yields a deflectogram (Fig. 2B), the beam profile (in the plane of deflection) plotted versus delay of the electron pulse with respect to the terahertz field. At the zero crossings of the field, the deflection is a steep function of time, and the beam width increases because of the finite-duration electron pulse. Raw images of the electron beam were recorded on the phosphor-covered camera with the terahertz deflecting field switched on and off and timed so as to yield maximum streaking of the beam (Fig. 2A). At the maxima and minima, minimal spreading occurs. The electron pulse duration and the time-dependent optical forces are determined by fitting the data of Fig. 2B assuming an instantaneous momentum transfer transverse to the electron beam induced by the terahertz field as a function of the electron arrival time.

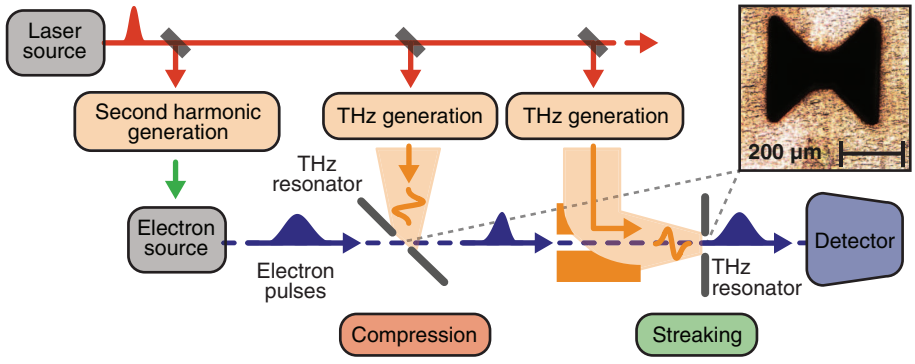

Fig. 1. Experimental setup. A 1-ps laser pulse from a Yb:YAG regenerative amplifier is frequency-doubled and generates an electron pulse from a thin-film gold photocathode. The laser also drives two optical-rectification stages, each generating single-cycle terahertz pulses with energy of up to 40 nJ. (Inset) Terahertz resonator structures are laser-machined in a 30-μm-thick aluminum foil. A first element, used for compression, is oriented at 45° to the electron beam, providing time-dependent longitudinal forces on the electrons. The second terahertz resonator, used for streaking, is oriented normal to the beam, resulting in time-dependent transverse deflection.

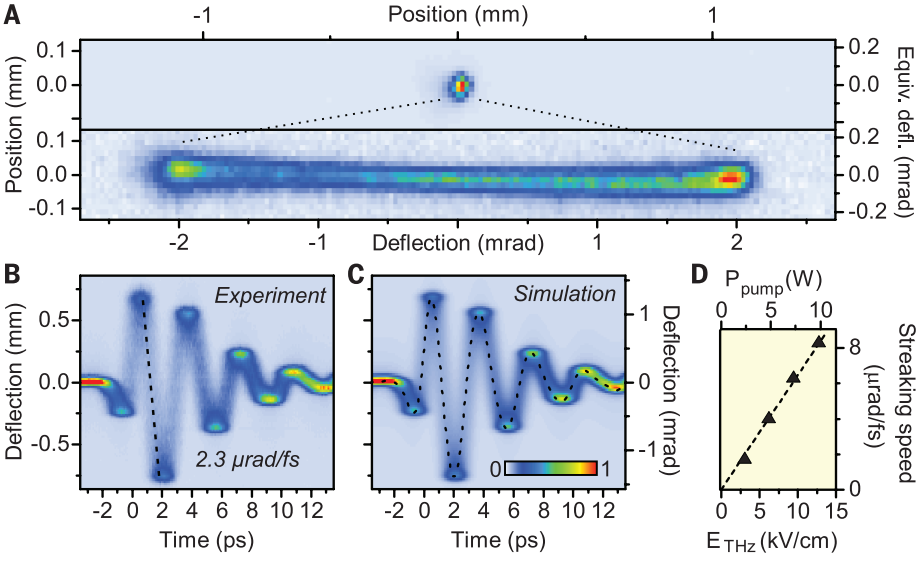

Fig. 2. All-optical terahertz streak camera. (**A**) Images of the electron beam on the camera with and without the terahertz field. The FWHM of the streaked beam is ~50 times larger than that of the unstreaked spot. (**B**) Time-dependent deflection (deflectogram) measured by varying the delay between the electron pulse and the streaking terahertz. Images of the beam are integrated along the unstreaked direction so as to determine a one-dimensional profile at each time delay. (**C**) Simulated deflectogram, result of a fit simultaneously characterizing the electron pulse duration and the streaking field (dotted line). The fitted electron pulse duration is 930 fs. (**D**) Streaking speed versus input terahertz field strength. The linear relationship supports a direct, field-driven interaction.

The deflection is proportional to the integral of the Lorentz force along the electron's trajectory and closely follows the electric field's temporal profile inside the slit because of near-field confinement, as a consequence of the electron traversing the field-enhanced region within a tiny fraction of the field oscillation period (*22*, *29*). This is in sharp contrast with attosecond streaking, which operates in the opposite limit (transit time much longer than the streaking field duration) so that the streaking spectrogram mimics the vector potential of the streaking field (*30*). A spline interpolation through four support points per picosecond is used for modeling time-dependent deflection, and a Gaussian temporal profile is assumed for the electron pulse. The calculated deflectogram with the fitted time-dependent deflection is shown in Fig. 2C. The electron pulse duration is 930 fs at full width at half maximum (FWHM), which is consistent with a propagation-induced temporal spread resulting from a 0.6-eV initial energy spread of the electron pulse.

The deflectogram displays sustained deflection oscillations far beyond the duration of the near-single-cycle incident terahertz driving pulse. The best fit yields a resonance frequency of 0.29 ± 0.01 terahertz of the resonator with a decay rate of 4.5 ± 0.4 ps resulting from radiative and resistive damping.

The resultant maximum streaking speed as a function of incident peak terahertz field strength in this range is shown in Fig. 2D. The highest value measured exceeds 8 μrad/fs, corresponding to a streaking speed of 4.4 μm/fs at the camera in our experimental geometry. The distance over which all momentum change accumulates is determined by the terahertz near-field decay length (~100 μm) and the foil thickness (~30 μm). The resulting interaction length is some 100 times smaller than in conventional streak cameras (*3*, *4*), removing a substantial limitation of their temporal resolution.

In the terahertz field–driven streak camera, temporal resolution is dictated by the beam quality and signal-to-noise ratio. At an incident terahertz field strength of 1.3×10^6 V/m, the RMS beam width on the camera of 1.6 pixels (25 μm) corresponds to 6-fs resolution (RMS). With ~1000 detected electrons, the beam quality and signal-to-noise ratio allow detection of displacements or spot width changes of 0.1 pixels (1.56 μm). A displacement of 0.1 pixels corresponds to 0.4 fs accuracy of arrival time measurements, whereas a 0.1-pixel increase of the spot size from the unstreaked value corresponds to a 2-fs (RMS) or ~4.5-fs (FWHM) pulse duration. These resolutions are achieved with a signal accumulation

time of 6 s and improve with longer integration. These values represent a near-two-order-of-magnitude improvement over the state of the art of microwave streak cameras (*3*, *4*), obtained already at terahertz fields of ~10^6 V/m as opposed to 10^{10} V/m available (*16*). As a consequence, our terahertz streaking concept may allow the direct measurement of subfemtosecond electron pulses (*31*, *32*) and their timing drifts.

Compression and measurement

Streaking deflectograms are shown in Fig. 3, A and B, with and without terahertz field compression, respectively. In the latter, the terahertz field strength of the compression stage has been adjusted to produce a temporal focus at the streaking stage. A pronounced sharpening of the trace can be seen in the vertical (streaking) direction, indicating a substantial reduction in electron pulse duration.

The systematic evolution of measured electron temporal profile for a varying compression strength g_E is shown in Fig. 3C (*33*). The deflection as a function of time is reconstructed and used to perform the nonlinear transformation between the spatial profile of the streaked pulse and the underlying temporal profile of the terahertz field–manipulated incident pulse (*24*). The dotted lines depict the results of three-dimensional electron trajectory simulations (*33*).

The electron pulse (Fig. 3C, blue) first shortens to a minimum duration (Fig. 3C, fifth trace from bottom) and afterward lengthens again, with a double-peaked shape that is characteristic of overcompression by a sinusoidal field (*31*). The experimental and theoretical pulse durations versus terahertz-field strength and average power of the driving laser are shown in Fig. 3D. The shortest pulse (Fig. 3D, inset) has a FWHM duration of 75 fs, which is in excellent agreement with the simulation and a factor of 12 shorter than the original, 930-fs pulses and shorter than the half period of many fundamental phonon modes and molecular vibrations. Comparison of the shortest measured pulse shape with a Gaussian profile (dotted line) reveals a deviation; this is a consequence of the terahertz field's residual curvature over the time scale of the incoming, uncompressed electron pulse. Optimized electron sources with sub-100-fs duration (*34*) will reduce this effect; the particle-tracing simulations (*24*) show that 3-fs (FWHM) compressed pulses can be generated with a smaller source size and the 100-fs incoming pulses achievable if the photoemission energy is matched to the work function (*7*, *27*). This would be an order of magnitude shorter than the 28-fs (FWHM) pulses generated in the single-electron regime so far (*28*) and allow the study of light-driven electronic motion via subcycle diffraction (*35*, *36*).

Electron-laser timing metrology

Femtosecond pump-probe crystallography with electrons (*7*) or with x-ray free-electron lasers (*1*, *2*) suffers from laser-electron timing jitter at the sample location, which is typically caused by imperfect laser-microwave synchronization (*10*, *11*). In contrast to the statistical electronic processes in the photodiodes used for microwave synchronization (*9*), laser-generated terahertz fields are, within the attosecond response time of the underlying nonlinear polarization, perfectly locked in time to the intensity profile of the pump pulses. Timing jitter/drift between the laser pump pulse and the electron probe pulse can only originate from extrinsic effects, such as fluctuations in path lengths or laser pulse energy.

Experimentally, we studied drifts of the electron pulse with respect to the terahertz field by setting the near-field–enhanced streak camera to a constant delay and recording the beam deflection over time (Fig. 4A). First, we scrutinized a possible role of amplitude-to-timing conversion in the nonlinear optical rectification process. The change in electron–terahertz field timing when varying the laser pump pulse intensity before the terahertz generation crystal is shown in Fig. 4B. We observed a systematic change in timing, but the slope at the operation conditions (7 W) is only 1.0 fs per 1% change in laser power, which is negligible for our laser system, whose intensity drifts and shot-to-shot energy fluctuations are below 2% (*25*).

In a second experiment, we measured drifts of the photoemission electrons with respect to the streaking terahertz field by turning the terahertz control field off. For integration times longer than 1 s, we obtained 4.6 fs (RMS) over 15 min (Fig. 4C). Last, we repeated this measurement with the terahertz-driven pulse compression activated; with integration times of 6 s, and after ~2 hours of laboratory thermalization, we measured 3.7 fs RMS over 3 hours (Fig. 4E). This vastly outperforms the long-term stability of state-of-the-art laser-microwave synchronization with feedback loops (*7*) and also compares favorably with the record value (5 fs RMS) achieved with direct microwave extraction from a laser pulse train and data post-processing (*9*). We expect that the measured, residual 3.7-fs drift could be further decreased by minimizing the (currently meter-scale) optical path lengths and/or stabilizing them interferometrically. Synchronization in the all-optical scheme is entirely single-pulse–based, and therefore, few-femtosecond stability can be maintained at any—and especially at very low—laser repetition rate. A clock or master oscillator is not required.

Direct terahertz-electron interaction at a foil

Enhancement of the terahertz field by a microstructure resonator has proven highly beneficial for electron pulse control and metrology, but some experiments might require more direct control,

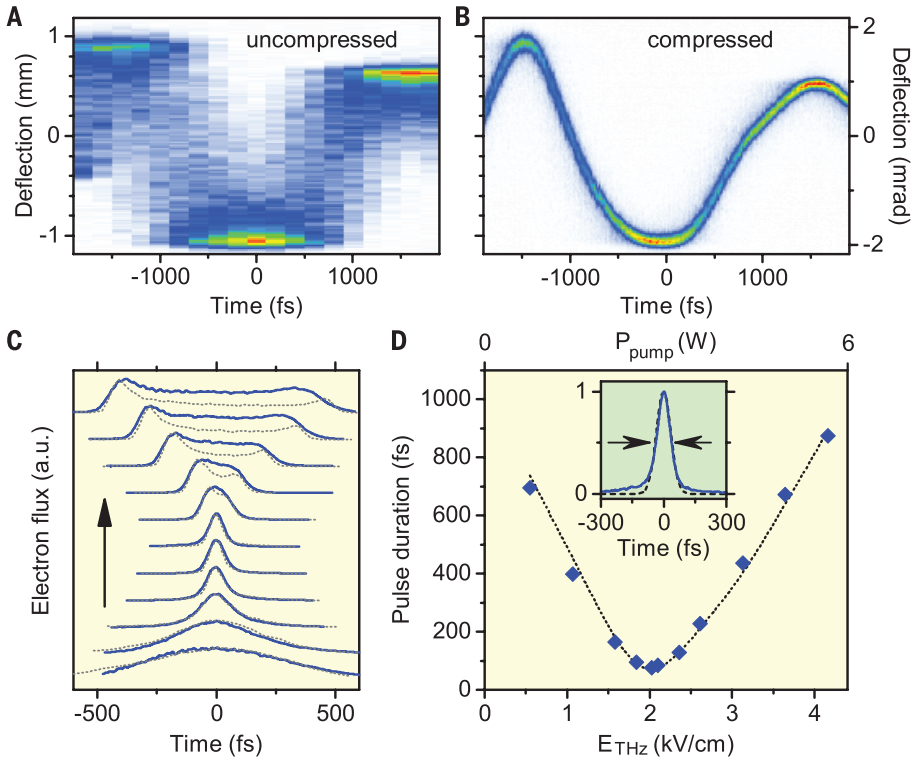

Fig. 3. Terahertz-driven electron pulse compression. (**A** and **B**) Comparison of deflectograms for (A) uncompressed (930 fs) and (B) compressed (75 fs) pulses at time steps of 200 and 10 fs, respectively. The deflectograms were measured sequentially and have a temporal resolution of ~9 fs (RMS). (**C**) Measured temporal profiles of the electron pulses (blue traces) as the compression strength is increased (black arrow), taking into account for long pulses the curvature of the time-dependent deflection. Simulated temporal profiles (10^4 particle trajectories) (*24*) are superimposed (dotted black lines). Differences between the measured and simulated pulses are due in part to the curvature of the streaking field, which reduces the streaking time-resolution at times far from zero. (**D**) Electron pulse duration (FWHM) versus incident terahertz field strength and optical pump power. The measured values are plotted as blue diamonds, and the simulation is shown as a dotted black line. (Inset) The shortest measured pulse profile [fifth trace from the bottom of (C)].

avoiding the localization and limited spectral response inextricably linked to resonators. For a direct electron-terahertz interaction, we realized a resonator-free interaction geometry based on a symmetry-breaking surface (*29*, *37*). In the depicted concept (Fig. 5A), a thin metal foil (70-nm aluminum) acts as a mirror for terahertz radiation, and electrons transmitted through it experience an abrupt extinction of the electromagnetic field, leading to net deflection. The combination of angles is chosen so that extended beam profiles experience a homogeneous time dependence owing to lateral phase matching (*29*).

Measured and calculated streaking deflectograms of an uncompressed electron pulse are depicted in Fig. 5, C and D, at an energy of 90 keV, exhibiting excellent agreement. Although the peak deflection is smaller than for the resonator-based setting, the deflectogram clearly exhibits single-cycle behavior, preserving the incident terahertz pulse's ultrabroadband spectrum without alteration (*25*). The peak-to-peak deflection as a function of the incoming terahertz field strength is shown in Fig. 5B, revealing the expected linear dependence. Electrons delivered in a nearly collimated beam are directly (and spatially uniformly) deflected directly with the field cycles, advancing the century-old cathode-ray-tube oscilloscope to the terahertz domain. Owing to the 1-fs-scale timing accuracy of the sampling electron pulse, the cut-off frequency of this terahertz cathode-ray oscilloscope is dictated by the inverse electron pulse duration, which is >10 THz with the demonstrated compressed pulses, >100 THz with the few-femtosecond electron pulses predicted by the simulations, and >1 PHz with the isolated attosecond electron pulses feasible with multistage compression.

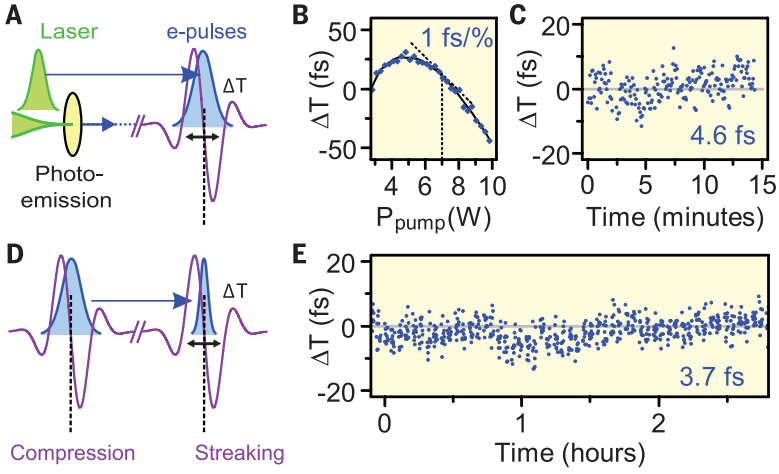

Fig. 4. Passive few-femtosecond synchronization. (**A**) Concept for measuring arrival-time drifts between the uncompressed electron pulses and the optical streaking field. (**B**) Systematic coupling of laser fluctuations to timing drifts. Measuring shifts in the terahertz zero-crossing time with increasing laser pump power reveals a slope of less than 1 fs per 1% change in laser power in a wide range of operation conditions. (**C**) Measured timing drift between photoemitted electron pulses and the terahertz field cycles at 10-s intervals. The integration time for each data point is 1 s. (**D**) Concept for measuring the arrival-time drift between terahertz-compressed electron pulses and the streaking field cycles. (**E**) Result with 6-s integration times reveals passive longer-term synchronization. The jitter values in (C) and (E) are RMS deviations; statistical errors are 3.5 and 2.7 fs, respectively.

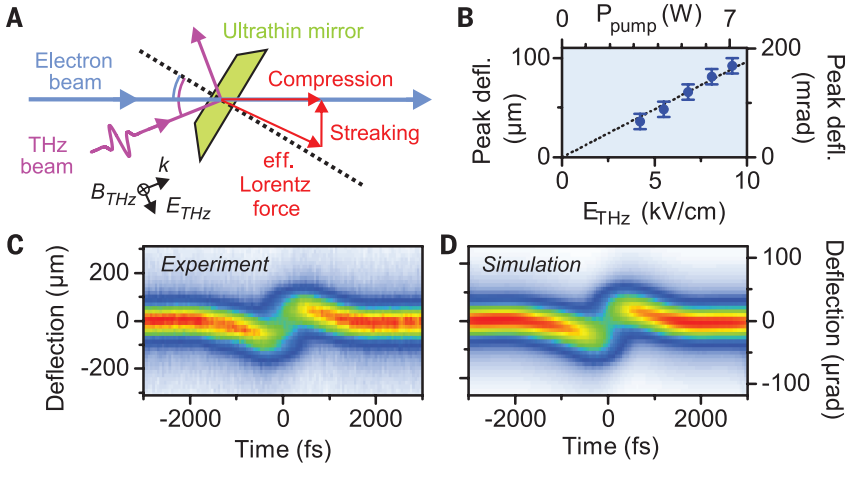

Fig. 5. Resonance-free single-cycle streaking. (**A**) Resonator-free concept for mediating the electron-terahertz interaction by using an ultrathin terahertz mirror. The angles of the terahertz and the electron beams with respect to the foil's surface normal (dotted line) are chosen for lateral phase matching across arbitrarily large electron and terahertz beam profiles. (**B**) Measurement of peak deflection versus incident terahertz field strength. (**C**) Experimental deflectogram revealing single-cycle behavior. (**D**) Simulated deflectogram with an electron pulse duration of 800 fs.

Conclusions and outlook

Our demonstrated generic and scalable all-optical methodology for the control and characterization of ultrafast electron pulses used laser-generated subcycle terahertz transients for 12-fold electron pulse compression, followed by temporal profile characterization with 10-fs resolution. Electron-transparent foils mediating the electron-field interaction permit time-energy phase-space manipulation of collimated electron beams of any size and, conversely, the temporal characterization of optical field transients up to frequencies only limited by the electron pulse duration, which—as opposed to the photon pulse in electro-optical sampling—may be shortened to <1 fs (*27*). Alternatively, resonant structures dramatically lower the terahertz power by a factor >1000 for effective compression and characterization of ultrashort electron pulses. Whereas the former opens the prospect of a petahertz-bandwidth cathode-ray oscilloscope as an alternative to attosecond photon-pulse metrology (*30*), the latter may lead to unprecedented spatiotemporal resolutions in pump-probe electron diffraction and imaging.

The moderate field strengths applied in our experiment offer the potential for increasing the interaction strengths by more than two orders of magnitude, limited by the high values of electrical breakdown at terahertz frequencies. This will result in correspondingly reduced propagation distances between subsequent terahertz control stages, which in turn should improve the passive few-femtosecond timing stability into the subfemtosecond regime. Simultaneous compression of 100-fs-scale input electron pulses to near-1-fs duration will permit spatiotemporal imaging of the fastest structural and infrared field–driven electron dynamics in molecular systems (*36*) as well as condensed matter (*35*) through single-electron diffraction (*38*) or microscopy (*6*) and allow measuring microscopic/atomic-scale electric field waveforms up to frequencies of visible light.

The demonstrated all-optical control may also be helpful for manipulating ultrabright multielectron bunches. Compact electron guns have demonstrated sub-200-fs electron pulses with sufficient charge for single-shot structural dynamics studies (*7*). Our concept is directly applicable to them as well. Alternatively, single-shot ultrafast electron diffraction may be advanced into the few-femtosecond regime and possibly beyond by terahertz-streaking 100-fs-scale probe pulses after passage through the sample (*4*). The unprecedented

temporal resolution of the terahertz-driven streak camera could also be used to characterize electron microbunching in free-electron lasers, supplementing terahertz-based diagnostics for the x-ray output (*39*, *40*). The demonstrated concept is scalable to higher terahertz frequencies and multiple stages, offering the potential for cascaded compression into the subfemtosecond regime or direct injection into a single optical cycle of a laser-field accelerator (*12*). This may, in the long run, lead to isolated attosecond electron pulses for recording dynamic changes of electron distribution in complex systems, including biological molecules and solid-state nanostructures.

REFERENCES AND NOTES

1. W. Ackermann *et al.*, *Nat. Photonics* **1**, 336–342 (2007).
2. P. Emma *et al.*, *Nat. Photonics* **4**, 641–647 (2010).
3. G. H. Kassier *et al.*, *Rev. Sci. Instrum.* **81**, 105103 (2010).
4. C. M. Scoby, R. K. Li, E. Threlkeld, H. To, P. Musumeci, *Appl. Phys. Lett.* **102**, 023506 (2013).
5. C. Kealhofer *et al.*, *Opt. Lett.* **40**, 260–263 (2015).
6. D. J. Flannigan, A. H. Zewail, *Acc. Chem. Res.* **45**, 1828–1839 (2012).
7. G. Sciaini, R. J. D. Miller, *Rep. Prog. Phys.* **74**, 096101 (2011).
8. J. Tenboer *et al.*, *Science* **346**, 1242–1246 (2014).
9. M. Walbran, A. Gliserin, K. Jung, J. Kim, P. Baum, *Phys. Rev. Appl.* **4**, 044013 (2015).
10. S. Schulz *et al.*, *Nat. Commun.* **6**, 5938 (2015).
11. G. J. H. Brussaard *et al.*, *Appl. Phys. Lett.* **103**, 141105 (2013).
12. R. J. England *et al.*, *Rev. Mod. Phys.* **86**, 1337–1389 (2014).
13. E. Hemsing, G. Stupakov, D. Xiang, A. Zholents, *Rev. Mod. Phys.* **86**, 897–941 (2014).
14. E. Esarey, C. B. Schroeder, W. P. Leemans, *Rev. Mod. Phys.* **81**, 1229–1285 (2009).
15. M. C. Hoffmann, J. A. Fülöp, *J. Phys. D Appl. Phys.* **44**, 083001 (2011).
16. M. Shalaby, C. P. Hauri, *Nat. Commun.* **6**, 5976 (2015).
17. S. D. Vartak, N. M. Lawandy, *Opt. Commun.* **120**, 184–188 (1995).
18. R. B. Yoder, J. B. Rosenzweig, *Phys. Rev. ST Accel. Beams* **8**, 111301 (2005).
19. L. J. Wong, A. Fallahi, F. X. Kärtner, *Opt. Express* **21**, 9792–9806 (2013).
20. J. Fabiańska, G. Kassier, T. Feurer, *Sci. Rep.* **4**, 5645 (2014).
21. S. R. Greig, A. Y. Elezzabi, *Appl. Phys. Lett.* **105**, 241115 (2014).
22. L. Wimmer *et al.*, *Nat. Phys.* **10**, 432–436 (2014).
23. E. A. Nanni *et al.*, *Nat. Commun.* **6**, 8486 (2015).
24. Materials and methods are available as supplementary materials on *Science* Online.
25. W. Schneider *et al.*, *Opt. Lett.* **39**, 6604–6607 (2014).
26. F. J. García de Abajo, M. Kociak, *New J. Phys.* **10**, 073035 (2008).
27. E. Fill, L. Veisz, A. Apolonski, F. Krausz, *New J. Phys.* **8**, 272 (2006).
28. A. Gliserin, M. Walbran, F. Krausz, P. Baum, *Nat. Commun.* **6**, 8723 (2015).
29. F. O. Kirchner, A. Gliserin, F. Krausz, P. Baum, *Nat. Photonics* **8**, 52–57 (2014).
30. R. Kienberger *et al.*, *Nature* **427**, 817–821 (2004).
31. P. Baum, A. H. Zewail, *Proc. Natl. Acad. Sci. U.S.A.* **104**, 18409–18414 (2007).
32. A. Feist *et al.*, *Nature* **521**, 200–203 (2015).
33. General Particle Tracer code (www.pulsar.nl/gpt) .
34. J. Hoffrogge *et al.*, *J. Appl. Phys.* **115**, 094506 (2014).
35. V. S. Yakovlev, M. I. Stockman, F. Krausz, P. Baum, *Sci. Rep.* **5**, 14581 (2015).
36. H. C. Shao, A. F. Starace, *Phys. Rev. Lett.* **105**, 263201 (2010).
37. T. Plettner *et al.*, *Phys. Rev. Lett.* **95**, 134801 (2005).
38. S. Lahme, C. Kealhofer, F. Krausz, P. Baum, *Struct. Dyn.* **1**, 034303 (2014).
39. U. Frühling *et al.*, *Nat. Photonics* **3**, 523 (2009).
40. I. Grguraš *et al.*, *Nat. Photonics* **6**, 852 (2012).

ACKNOWLEDGMENTS

This work was supported by the European Research Council and the Munich-Centre for Advanced Photonics. We thank D. Frischke for preparing ultrathin aluminum foils. The authors declare no competing financial interests.

SUPPLEMENTARY MATERIALS

www.sciencemag.org/content/352/6284/429/suppl/DC1
Materials and Methods
Fig. S1
References (*41*–*43*)

4 December 2015; accepted 2 March 2016
10.1126/science.aae0003

REPORTS

ORGANIC CHEMISTRY

Catalytic asymmetric addition of Grignard reagents to alkenyl-substituted aromatic *N*-heterocycles

Ravindra P. Jumde, Francesco Lanza, Marieke J. Veenstra, Syuzanna R. Harutyunyan*

Catalytic asymmetric conjugate addition reactions represent a powerful strategy to access chiral molecules in contemporary organic synthesis. However, their applicability to conjugated alkenyl-*N*-heteroaromatic compounds, of particular interest in medicinal chemistry, has lagged behind applications to other substrates. We report a highly enantioselective and chemoselective catalytic transformation of a wide range of β-substituted conjugated alkenyl-*N*-heteroaromatics to their corresponding chiral alkylated products. This operationally simple methodology can introduce linear, branched, and cyclic alkyl chains, as well as a phenyl group, at the β-carbon position. The key to this success was enhancement of the reactivity of alkenyl-heteroaromatic substrates via Lewis acid activation, in combination with the use of readily available and highly reactive Grignard reagents and a copper catalyst coordinated by a chiral chelating diphosphine ligand.

The majority (88%) of all known active pharmaceutical ingredients (APIs) contain functionalized heterocyclic aromatic rings with a preponderance of *N*-containing aromatic heterocycles (*1*). Furthermore, approximately half of all APIs are chiral (*1*). Because the two enantiomers of a chiral drug can exhibit markedly different bioactivity, any new chiral API must be produced as a single enantiomer. Catalytic asymmetric carbon-carbon (C-C) bond formation represents the most straightforward and atom-efficient strategy for the construction of organic chiral molecules (*2*–*4*). Organometallic reagents are used in a substantial fraction of the C-C bond–forming reactions used to construct API molecules (*5*–*7*). The conjugate addition of organometallic reagents to electron-deficient substrates (Michael acceptors) has proven to be a powerful method for creating new C-C bonds in a catalytic asymmetric manner for more than 20 years (*7*–*12*). In this context, the catalytic asymmetric addition of organometallics to conjugated alkenyl-heteroaromatic compounds represents an attractive strategy to access valuable chiral heterocyclic aromatic compounds in enantiopure form. Addition of carbon nucleophiles to conjugated vinyl-substituted heteroaromatic compounds, leading mainly to achiral molecules, is well known (*13*, *14*). In contrast, there are only a handful of reports of nucleophilic additions to β-substituted analogs, in particular when organometallics are considered.

An early attempt at such a catalytic asymmetric reaction, reported in 1998, was the nickel-catalyzed addition of Grignard reagents to substituted 4-(1-alkenyl)pyridines (*15*). Although the reaction did not appear to be ligand-accelerated and provided only 0 to 15% enantiomeric excess (ee), these results suggested that catalytic asymmetric versions of such transformations were feasible. It was not until 2010 that a highly enantioselective, Rh-catalyzed addition of an organometallic reagent to alkenyl-substituted heteroaromatic compounds—namely arylation with an arylboronic acid—was realized, furnishing a wide range of chiral products with high yields and enantioselectivities (*16*–*19*).

The limited number of reports on transition metal–catalyzed asymmetric conjugate addition of nucleophiles to β-substituted alkenyl-heteroaromatic compounds, restricted to precious metal–catalyzed arylations, is in striking contrast to the plethora of methodologies available for the catalytic asymmetric alkylations, arylations, alkynylations, and allylations of common Michael acceptors, activated by carbonyl, nitrile, sulfonyl, and nitro groups (*8*–*12*). The paucity of methodologies for the nucleophilic addition to β-substituted alkenyl-heteroaromatic compounds is rooted in the intrinsically lower reactivity of these compounds, due to the relatively weak activation from the heteroaromatic moiety (*13*, *14*). Furthermore, the numerous examples of nonasymmetric additions to vinyl-substituted heteroaromatic compounds indicate that the presence of a β-substituent decreases the reactivity further, presumably because of the steric hindrance it introduces.

We decided to explore the addition of Grignard reagents to β-substituted conjugated alkenyl-heteroaromatic compounds. Inexpensive and readily available Grignard reagents are some of the most commonly used organometallics in synthetic chemistry (*20*), especially in copper-catalyzed asymmetric conjugate addition to a variety of Michael acceptors (*9*–*12*). We reasoned

Stratingh Institute for Chemistry, 9747 AG Groningen, Netherlands.
***Corresponding author. Email: s.harutyunyan@rug.nl**

Editor's Summary

Electron pulses under control

The ability to take snapshots of fast events can often provide insights into the dynamics of the processes involved: chemical reactions, electronic transport, structural transitions, and complex combinations involving of all of these processes. Kealhofer *et al.* describe an ultrafast optics approach for generating bunches of electrons and compressing them by more than an order of magnitude to just femtosecond time scales (see the Perspective by Ropers). The technique opens up the possibility of imaging ultrafast phenomena with atomic-scale spatial resolution.

Science, this issue p. 429; see also p. 410